Journal of Colloid and Interface Science 528 (2018) 18–26

Contents lists available at ScienceDirect

Journal of Colloid and Interface Science

journal homepage: www.elsevier.com/locate/jcis

Regular Article

Co@Pd core-shell nanoparticles embedded in nitrogen-doped porous carbon as dual functional electrocatalysts for both oxygen reduction and hydrogen evolution reactions

Hongyu Yang [a], Zhenghua Tang [a,b,*], Kai Wang [a], Wen Wu [a], Yinghuan Chen [a], Zhaoqing Ding [a], Zhen Liu [c], Shaowei Chen [a,d,*]

[a] Guangzhou Key Laboratory for Surface Chemistry of Energy Materials, New Energy Research Institute, School of Environment and Energy, South China University of Technology, Guangzhou Higher Education Mega Centre, Guangzhou 510006, China
[b] Guangdong Provincial Key Laboratory of Atmospheric Environment and Pollution Control, Guangdong Provincial Engineering and Technology Research Center for Environmental Risk Prevention and Emergency Disposal, School of Environment and Energy, South China University of Technology, Guangzhou Higher Education Mega Centre, Guangzhou 510006, China
[c] Department of Physics & Engineering, Frostburg State University, Frostburg, MD 21532-2303, United States
[d] Department of Chemistry and Biochemistry, University of California, 1156 High Street, Santa Cruz, CA 95064, United States

GRAPHICAL ABSTRACT

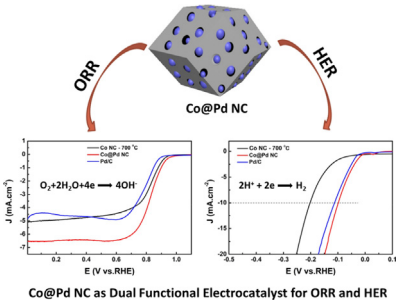

Co@Pd NC as Dual Functional Electrocatalyst for ORR and HER

ARTICLE INFO

Article history:
Received 1 January 2018
Revised 3 May 2018
Accepted 21 May 2018
Available online 21 May 2018

Keywords:
ZIF-67
Co@Pd core-shell nanoparticles
Nitrogen-doped porous carbon
Dual functional electrocatalysts
Oxygen reduction reaction
Hydrogen evolution reaction

ABSTRACT

Developing efficient bi-functional electrocatalysts for both oxygen reduction reaction (ORR) and hydrogen evolution reaction (HER) is crucial for producing hydrogen and utilizing hydrogen effectively to promote electrochemical energy storage in proton membrane exchange fuel cells (PEMFCs). Herein, we report Co@Pd core-shell nanoparticles encapsulated in porous carbon derived from zeolitic imidazolate framework 67 (ZIF-67) for both ORR and HER. The controlled pyrolysis of ZIF-67 can lead to the formation of Co nanoparticles encapsulated in nitrogen-doped porous carbon (Co NC), which subsequently underwent galvanic replacement with Na_2PdCl_4 to form Co@Pd core-shell nanoparticles embedded in nitrogen-doped porous carbon (Co@Pd NC). The Co@Pd NC exhibited outperformance in ORR and HER than commercial Pd/C, as manifested by more positive onset potential and larger diffusion-limited current density in ORR tests, as well as a small overpotential to drive a current density of 10 mA cm^{-2}, and much lower Tafel slope in HER tests. It also demonstrated more robust long-term stability than commercial Pd/C for both ORR and HER. Multiple techniques inter-confirmed that the Pd loading in the sample was very low. The findings can pave a path for fabricating a core-shell structured nanocomposite with ultralow noble

* Corresponding authors at: Guangzhou Key Laboratory for Surface Chemistry of Energy Materials, New Energy Research Institute, School of Environment and Energy, South China University of Technology, Guangzhou Higher Education Mega Centre, Guangzhou 510006, PR China (Z. Tang).
E-mail addresses: zhht@scut.edu.cn (Z. Tang), shaowei@ucsc.edu (S. Chen).

https://doi.org/10.1016/j.jcis.2018.05.063

metal usage as a bifunctional catalyst for electrochemical energy storage and conversion with high-efficiency and remarkable longevity.

1. Introduction

To mitigate and eventually resolve the global energy crisis and the severe environmental problem, it is crucial to develop sustainable and green energy technologies such as water splitting, fuel cell, metal-air batteries, and so on [1–3]. The oxygen reduction reaction (ORR) occurring at the cathode plays an important role in determining the energy transfer efficiency of fuel cells and metal air batteries [4–6], while hydrogen evolution reaction (HER) provides an efficient method for massively producing clean and renewable energy [7–9]. Therefore, the development of dual functional catalysts for both ORR and HER is highly desirable [10]. Presently, the state-of-art electrocatalysts are still Pt and Pt based alloys for both ORR and HER [11–13], mainly due to their low overpotentials and high energy densities. Unfortunately, Pt is a noble metal with limited reserve in the Earth's Crust hence significantly hindering the catalysts for large-scale commercialization. Furthermore, the Pt based electrocatalysts also suffer from low chemical stabilities for practical applications. To that end, developing earth-abundant materials with high efficiency and robust durability for both ORR and HER is of great fundamental importance and practical values for fuel cells, metal-air batteries, water splitting, and other renewable energy technologies.

Emerging as a new class of porous crystalline materials, metal-organic frameworks, made of organic ligands and metal ion center, have attracted tremendous attentions in the past two decades, thanks to their versatile applications in gas storage and/or separation [14,15], sensing [16], catalysis [17–19], drug delivery [20] and so on [21]. Recently, there is a rapid growing interest in developing MOF-based materials for energy conversion and storage [22–25], and MOFs have proved to be particularly suitable for electrochemical applications due to their tunable chemical composition, well-defined porous structure and high surface-to-volume ratio. Furthermore, MOFs have been widely served as a sacrificial precursor or template to fabricate porous carbon or nitrogen-doped porous carbon materials for electrocatalytic applications [26–29]. For instances, Zhang et al. reported that through a successive carbonization, catalytic graphitization, and nitridation process, MOF-5 can be transformed into nitrogen-doped porous carbon and carbon nanotubes with enhanced activity toward ORR [30]. While in another report, Wu group described that graphene tubes with nitrogen doping can be prepared through a high-temperature graphitization process from MIL-100, and high activity toward ORR in acid media was acquired [31]. Recently, Lai et al. developed an *in-situ* confinement pyrolysis strategy that can simply but efficiently transform ZIF-8 polyhedrons to nitrogen enriched meso-microporous carbon [32]. Through the calcination of Cu- and Mo-based MOFs, porous molybdenum carbide octahedra was prepared for HER in both acid and alkaline electrolytes [33]. By adopting a facile Cu-confined thermal conversion strategy of ZIF-67 pre-grown on Cu nanowires, Zheng group fabricated the Cu, Co-embedded *N*-enriched mesoporous carbon for both ORR and HER [34]. Such catalyst exhibited a half-wave potential as 0.884 V (vs. RHE, reversible hydrogen electrode) in ORR and a low overpotential of 145 mV (vs. RHE) at 10 mA cm^{-2} in HER, further demonstrating the great promises of MOFs derived materials to boost the two electrocatalytic reactions [34].

In a recent study, we reported Co@Pt core-shell nanoparticles encapsulated in porous carbon derived from zeolitic imidazolate framework 67 (ZIF-67) for ORR [35]. Note that, the controlled pyrolysis of ZIF-67 can lead to the formation of Co nanoparticles encapsulated in nitrogen-doped porous carbon, which subsequently underwent galvanic replacement with K_2PtCl_4 to form Co@Pt core-shell nanoparticles. On the basis of this work, herein, we demonstrated the fabrication of Co@Pd nanoparticle embedded in nitrogen-doped porous carbon derived from ZIF-67 for both ORR and HER.

2. Experimental section

2.1. Materials

Methanol and cobalt nitrate hexahydrate ($Co(NO_3)_2{\cdot}6H_2O$, 99.0%) were obtained from Damao Chemical Reagents (Tianjin, China). 2-Methylimidazole (MeIM, 98.0%), commercial Pd/C (10%) and disodium tetrachloropalladate (Na_2PdCl_4, 99.95%) were purchased from Energy Chemicals (Shanghai, China). Distilled water with a resistivity of 18.3 MΩ·cm was used in this work.

2.2. Synthesis of ZIF-67 nanocrystal

ZIF-67 nanocrystals were synthesized by following a procedure in previous reports [35,36]. In a typically reaction, 1.8 g of $Co(NO)_3{\cdot}6H_2O$ was first dissolved into 10 mL deionized water under magnetic stirring. Then, the above solution was added quickly into another solution, which was prepared by dissolving 22 g of 2-Methylimidazole in 70 mL deionized water. The mixed solution was kept stirring for at least 6 h at 800 rpm at room temperature, forming purple precipitates gradually. The precipitates were collected by centrifugation at 8000 rpm and washed by water and ethanol 3–5 times, respectively. The solid was dried at 50 °C for 24 h in a vacuum oven, yielding the purified ZIF-67 nanocrystals.

2.3. Synthesis of Co NC at different temperatures

The detailed process of preparing Co@Pd NC can be described as follows: 200 mg of the prepared ZIF-67 was transferred to a porcelain boat and pyrolyzed at 500 °C, 600 °C, 700 °C, 800 °C, 900 °C and 1000 °C for 2 h with a heating rate of 1 °C/min under continuous N_2 flow. When cooling to room temperature, the product was entitled as Co NC-x (x = 500 °C, 600 °C, 700 °C, 800 °C, 900 °C or 1000 °C), in which Co nanoparticles were embedded in nitrogen-doped porous carbon.

2.4. Synthesis of Co@Pd NC

Briefly, 50 mg of Co NC-700 °C was dispersed into 10 mL of deionized water in a round-bottom flask via ultra-sonication. Then 5 mL of water solution containing 10 mg Na_2PdCl_4 was added into the above dispersion slowly. The mixture was kept stirring at 1200 rpm for 12 h. The above process was conducted under Ar flow to prevent the oxidation of Co nanoparticles. The acquired black precipitates were washed by water and ethanol 3–5 times, and dried in a vacuum oven at 50 °C for ~12 h. The obtained solid was denoted as Co@Pd NC.

2.5. Characterizations

X-ray photoelectron spectroscopic (XPS) measurements were performed on a Phi X-tool instrument to probe the surface chemical compositions and valence states. Powder X-ray diffraction patterns (XRD) were conducted on a Bruker D8 diffractometer with Cu K_α radiation ($\lambda = 0.1541$ nm). Scanning electronic microscopic (SEM) images were performed with a field-emission scanning electron microscope (FESEM, Merlin) equipped with an energy dispersive X-ray spectroscopy (EDX). High-resolution transmission electron microscopic measurements (HR-TEM) were conducted with a transmission electron microscope (JEOL TEM-2010).

2.6. Electrochemical measurements

All electrochemical tests were conducted on an electrochemical workstation (CHI 750E, CH Instruments Inc, Shanghai, China) with a conventional three-electrode system at ambient temperature. For ORR measurements in the alkaline solution, a glassy carbon electrode (GCE), a Pt plate and a AgCl/Ag wire with saturated KCl (3.0 M) were employed as the working electrode, the counter electrode and the reference electrode, respectively. A glassy carbon electrode (GCE) coated with catalysts was polished with 0.05 and 0.3 μm alumina powders. For HER measurements in acid solution, a glassy carbon electrode (GCE), carbon rod and saturated calomel electrode (SCE) were employed as the working electrode, the counter electrode, and the reference electrode, respectively. Catalyst ink was prepared by the following process. For ORR, 2 mg of the sample was dispersed into 1.0 mL ethanol by sonication for 30 min. 10 μL of the above solution and 10 μL ethanol containing Nafion (20 μL/mL) was added on the GCE with a catalyst loading of 80.8 μg cm^{-2}. The Ag/AgCl reference electrode was calibrated against a reversible hydrogen electrode (RHE), $E_{RHE} = E_{Ag/AgCl} + 0.196\ V + 0.0592 * pH$. For HER, 5 mg of the sample was dispersed into 1.0 mL ethanol/water (v: v = 1:1) solution by sonication for 30 min. 5 μL of the above solution and 10 μL ethanol containing Nafion (20 μL/mL) was added on the GCE with a catalyst loading amount of 357.1 μg cm^{-2}. $E_{RHE} = E_{SCE} + 0.2415\ V + 0.0592 * pH$.

3. Results and discussions

3.1. Co@Pd Core-shell structure revealed by electron microscopic studies

In this study, zeolitic imidazolate framework 67 (ZIF-67) was first synthesized with cobalt nitrate and 2-methylimidazole at room temperature. The size and morphology of ZIF-67 were then observed by SEM (Fig. S1a and b). One can see that, ZIF-67 possessed a well-defined octahedral shape, in good consistence with the previous studies [37,38]. The series of Co NC-x (x = 500–1000 °C) samples were then obtained by calcinating ZIF-67 at different temperatures. Upon calcination of ZIF-67 at various temperatures (from 500 °C to 1000 °C), slight differences in morphology and surface structure can be easily identified. Under relatively lower temperatures (500 °C, 600 °C and 700 °C), uniform pore structures can still be found but slightly less-defined than ZIF-67 (Fig. S1c–e). While at higher temperatures (800 °C, 900 °C and 1000 °C, Fig. S1f–h), the defined skeleton began to collapse and heavy aggregation can be observed, especially for the sample calcinated at 1000 °C. Note that, such coalescence and aggregation may cause the significant decrease of specific surface area, hence not favorable for electrocatalytic reaction. The XPS survey scan spectra of ZIF-67 and the Co NC-x series are presented in Fig. S2, and it confirms the presence of C, N, O and Co elements.

Subsequently, the catalytic activity of the Co NC-x samples toward ORR was then tested by cyclic voltammetric (CV) and rotating ring-disk electrode (RRDE) measurements in O_2-saturated 0.1 M KOH solution from −0.04 V to 1.16 V (vs. RHE) at a scan rate of 10 mV s^{-1}. Fig. S3 shows cyclic and RRDE voltammograms of a glassy carbon electrode modified with Co NC-x (x = 500–1000 °C), and the results are also summarized in Table S1. The sample of Co NC-700 °C exhibited the highest cathodic peak position and the most positive onset potential among the series. Also, it displayed the largest diffusion-limited current density. The results indicate that Co NC-700 °C possessed the best electrocatlytic performance toward ORR, plus the preserved structural feature at this calcination temperature, 700 °C was chosen as the optimal temperature for pyrolysis for subsequent Co@Pd core-shell nanoparticle preparation.

The Co NC-700 °C sample was then subjected to galvanic displacement reaction with K_2PdCl_4 to form Co@Pd core-shell nanoparticles embedded in nitrogen-doped porous carbon (Co@Pd NC). Fig. S4 presents the typical SEM image of Co@Pd NC compared with ZIF-67 and Co NC-700 °C. It can be noted that, Co NC-700 °C and Co@Pd NC exhibited almost identical size, lower than that of ZIF-67 due to the calcination. In addition, ZIF-67 displayed well-defined dodecahedron but Co NC-700 °C and Co@Pd NC showed Blurred edges and a rough surface after calcination. Co@Pd NC preserved the structural features of Co NC-700 °C very well [35,36,39]. Consistent results can also be found in the XRD pattern between Co NC-700 °C and Co@Pd NC, as illustrated in Fig. S5. For both Co NC-700 °C and Co@Pd NC, there is a slightly broad diffraction peak located at $2\theta = 26.0°$, which can be attributed to the (0 0 2) crystalline planes from the graphitic carbon. In addition, there are three other defined peaks at $2\theta = 44.4°$, 51.6°, and 75.8°, which are ascribed to the (1 1 1), (2 0 0) and (2 2 0) crystalline planes from the metallic cobalt (JCPDS No. 15-0806). One may notice that, Co@Pd NC kept an almost identical pattern with Co NC-700 °C, mainly due to that fact that the Co NC skeleton was preserved upon the galvanic displacement reaction [35,36,39]. The results also suggest that Co nanoparticles were indeed formed and well embedded in the carbon matrix. Interestingly, there is no well-defined XRD pattern from Pd, probably due to the formation of the ultra-thin Pd shell, which will be discussed next.

The representative transmission electron microscopic (TEM) image and corresponding size distribution histograms of Co NC-700 °C and Co@Pd NC are shown in Fig. 1a,b. It can be observed that, the Co nanoparticles are uniformaly dispersed in porous carbon, and the average diameter of the Co nanoparticles in Co NC-700 °C and Co@Pd NC was calculated as 7.57 ± 1.81 nm and 7.81 ± 1.32 nm, respectively. Note that, the size and shape of the Co nanoparticles remained almost unchanged upon the galvanic displacement reaction. From the high resolution (HR) TEM image of Co@Pd NC (Fig. 1c), two types of well-defined lattice fringes with interplanar distance of 0.210 nm and 0.335 nm were observed, which are in good agreement with the Co(1 1 1) and C(0 0 2) crystal planes [35,40]. High-angle annular dark-field scanning transmission electron microscopic (HAADF-STEM) analysis was conducted to further probe the structural features and elemental distrbutions of the Co@Pd NC sample. From the low-magnification EDX images (Fig. 1d–h), it can be noted that C, N, Co and Pd were uniformly distributed in the sample of Co@Pd NC, and three-dimensional Pd elements are distributed in the interior of the Co@Pd NC particles. While the high-magnification EDX images (Fig. 1i–m) further disclose that, Co and Pd elements coexist in an individual particle, and surrounded by the nitrogrn-doped carbon. Co is located in the core with high concentration while Pd is scattered, indicating the potential formation of core-shell structure. Moreover, the line-scan profile (Fig. 1o) extrapolated from the marked line in the sample (Fig. 1n) illustrates that,

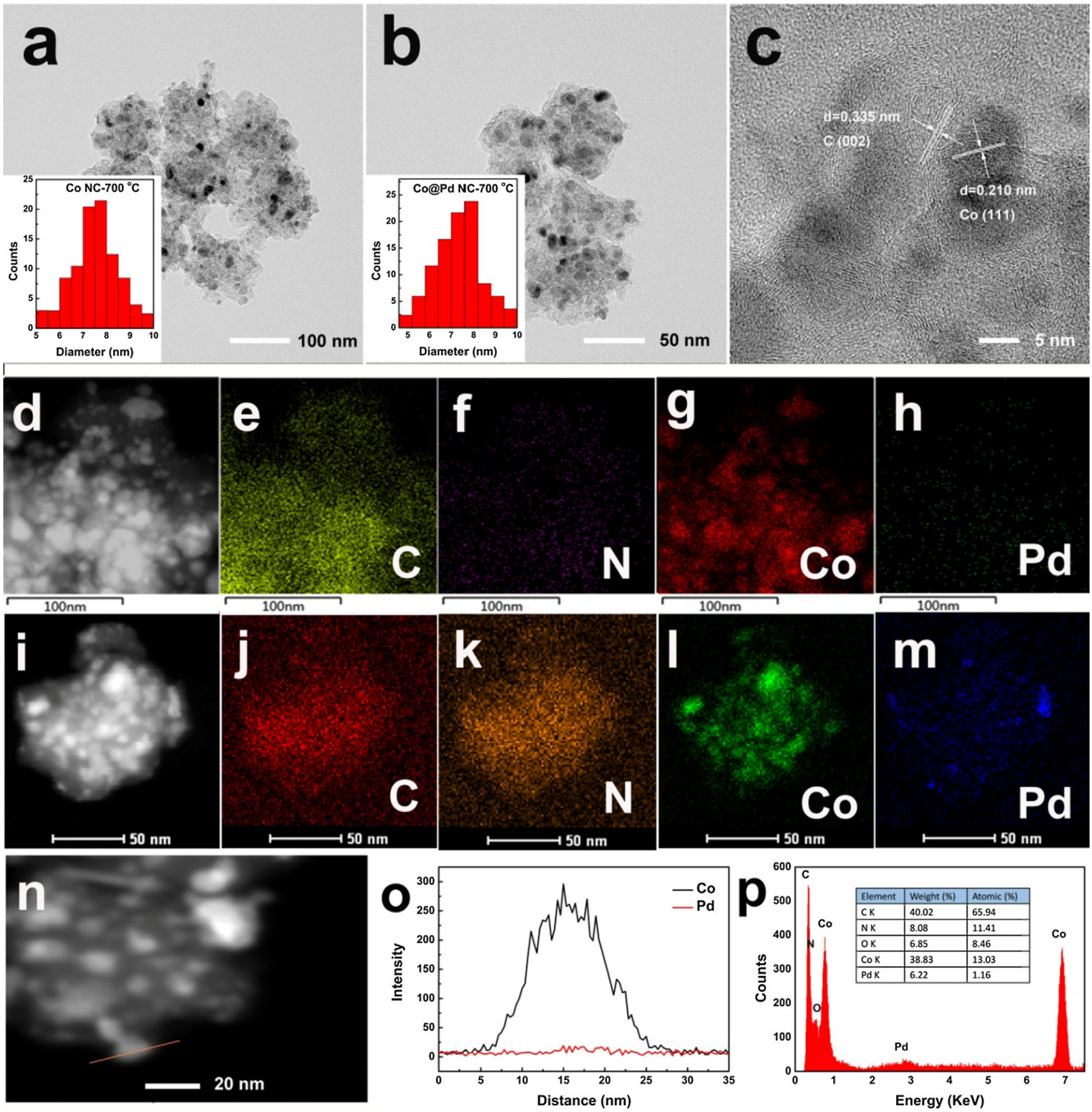

Fig. 1. Representative TEM images and corresponding size distribution histograms of cobalt nanoparticles in (a) Co NC-700 °C and (b, c) Co@Pd NC. Typical HAADF-STEM image of (d) Co@Pd NC and (e–h) the corresponding elemental maps (C, N, Co and Pd). Typical HAADF-STEM image of (i) Co@Pd NC and (j–m) the corresponding elemental maps (C, N, Co and Pd) with high magnification. (n) Line-scanning profiles of Co and Pd from the direction marked by a white line in (o). (p) Energy dispersive X-ray (EDX) spectrum of Co@Pd NC and the inserted table displays the elemental percentage of C, N, O, Co and Pd in Co@Pd NC.

Co showed a peak-shaped distribution where Pd was in a very low concentration, further attesting the formation of Co core and Pd shell structure. The EDX spectra of all the elements and calculated weight and atomic percentage from Co@Pd NC are presented in Fig. 1p. It can be noted that, the atomic percentage of Pd was as low as 1.16%, and the calculated Pd-to-Co atomic ratio is ~0.089.

3.2. XPS analysis

The chemical composition and valence states of the Co@Pd NC were then probed by X-ray photoelectron spectroscopy (XPS). The XPS survey scan spectra of ZIF-67, Co NC-700 °C and Co@Pd NC can be found in Fig. S6. The appearance of sharp Pd3d peak further attests that Pd elements were successfully incorporated into the sample of Co@Pd NC. In addition, from XPS measurement, the atomic percentage of all the elements from Co@Pd NC can be estimated, and they are compared with the results from EDX. The compared results are summarized in Table S2. The atomic percentages from XPS are close to the values from EDX, while the Pd-to-Co atomic ratio from XPS was 0.086, also in good consistence with the value from EDX (0.089). As both XPS and EDX measurements are surface-dependent techniques with only a few nanometers in

depth on the surface can be detected, to acquire more accurate atomic percentage values of the various elements, the inductively-coupled plasma-mass spectrometry (ICP-MS) was conducted and shown in Table S2 as well. It can be noted that, Co was atomically 6.64% in total while Pd exhibited an atomic percentage of only 0.61%.

The core-level XPS spectra of the Pd3d electrons from Pd/C and Co@Pd NC is presented in Fig. 2a. For both Pd/C and Co@Pd NC, the binding energy for $Pd3d_{5/2}$ and $Pd3d_{3/2}$ electrons can be deconvoluted into a pair of doublets. The peaks at lower energies of 335.9 eV and 341.1 eV are ascribed to metallic Pd, while the peaks at higher energies of 337.2 eV and 342.5 eV are assigned to Pd(II). The Pd element in Co@Pd NC was calculated to be consist of 15.1% Pd(0) and 84.9% Pd(II), while in Pd/C, the Pd component include 77.6% Pd(0) and 22.4% Pd(II). Note that, previous studies have shown that the existence of Pd(II) is probably favorable for facilitating the kinetics of electrocatalytic reactions [41–43]. Fig. 2b presents the core-level XPS spectra of the $Co2p_{3/2}$ electrons of Co NC-700 °C and Co@Pd NC. The broad peak can be deconvoluted into a pair of peaks for both samples, the binding energy at 778.6 eV is ascribed to metallic Co species, while the binding energy at 781.2 eV can be assigned to the Co^{2+} species for Co NC-700 °C and Co@Pd NC. The Co^{2+} species in Co NC-700 °C might be arisen from the surface Co atoms interacting with the carbon matrix [44]. Compared with Co NC-700 °C (54.7% Co(0), 45.3% Co(II)), the atomic percentages for metallic Co and Co^{2+} from Co@Pd NC is 19.9% and 80.1%, respectively. The significant enhancement of Co(II) species in Co@Pd NC indicates that, electron transfer behaviors probably occurred from Co atoms to Pd atoms.

3.3. The ORR performance of Co@Pd NC

Subsequently, the electrocatalytic performance toward ORR for Co@Pd NC was examined and compared with Co NC-700 °C and commercial Pd/C. The ORR performance of the three samples are compiled in Table 1. As illustrated in the cyclic voltagramms in Fig. 3a, in oxygen-saturated 0.1 M KOH solution, a sharp peak at around 0.7–0.85 V attributed to oxygen reduction can be found for all three samples, implying effective catalytic activity. However, the sample of Co@Pd NC exhibited the largest cathodic peak current, suggesting a superior catalytic performance. Fig. 3b depicts the RRDE voltagramms of the three samples, whereas the onset potential and diffusion-limited current density (at +0.5 V) can be estimated as 0.94 V and $-4.83\ mA\ cm^{-2}$, 0.95 V and $-4.66\ mA\ cm^{-2}$, and 0.97 V and $-6.50\ mA\ cm^{-2}$ for Pd/C, Co NC-700 °C, and Co@Pd NC, respectively. Both the onset potential and diffusion-limited current density of Co@Pd NC are higher than the Co NC-700 °C precursor and the benchmark Pd/C catalyst. With the presence of a little amount of Pd, the enhancement of ORR activity can be observed in Co@Pd NC. In addition, to further elucidate the reaction kinetics for Co@Pd NC, RRDE measurements with different rotation rates from 400 rpm to 2500 rpm were then conducted and shown in Fig. 3c. One may notice that, the current density increased with the increase of the rotation rate. The corresponding Tafel K-L plots for Co@Pd NC and Pd/C are shown in Fig. 3d and e. Note that, a great linearity with a rather consistent slope was exhibited for both Co@Pd NC and Pd/C, indicating that both samples adopted a first-order reaction kinetics with regard of dissolved oxygen concentration in solution. Furthermore, the Tafel plots of the three samples are shown in Fig. 3f, and the corresponding Tafel slopes were then calculated. Co@Pd NC displayed a Tafel slope of 37.1 $mV\ dec^{-1}$, lower than that of Co NC-700 °C, suggesting a faster reaction kinetics. The Tafel slope value of Co@Pd NC is comparable with that of commercial Pd/C, and also agrees well with the values from Pd-based nanomaterials or nanostructured Pd materials coated electrodes [45–49]. It implies that, same with Pd/C, the rate determining step is probably the first electron transfer to oxygen molecule during the electrocatalytic process for Co@Pd NC [50–53].

The long-term stability of the Co@Pd NC sample was then assessed and compared with Co NC-700 °C and Pd/C by accelerated durability tests (ADT), which was conducted by cycling the catalysts over the potential range from 0 to +1.10 V at $10\ mV\ s^{-1}$ in an oxygen-saturated 0.1 M KOH solution. As depicted in Fig. 4a and c, after 5000 cycles of potential scans, the half-wave potential of Co NC-700 °C and Pd/C shifted about ~24 mV and ~14 mV, respectively, while in sharp contrast, the sample of Co@Pd NC

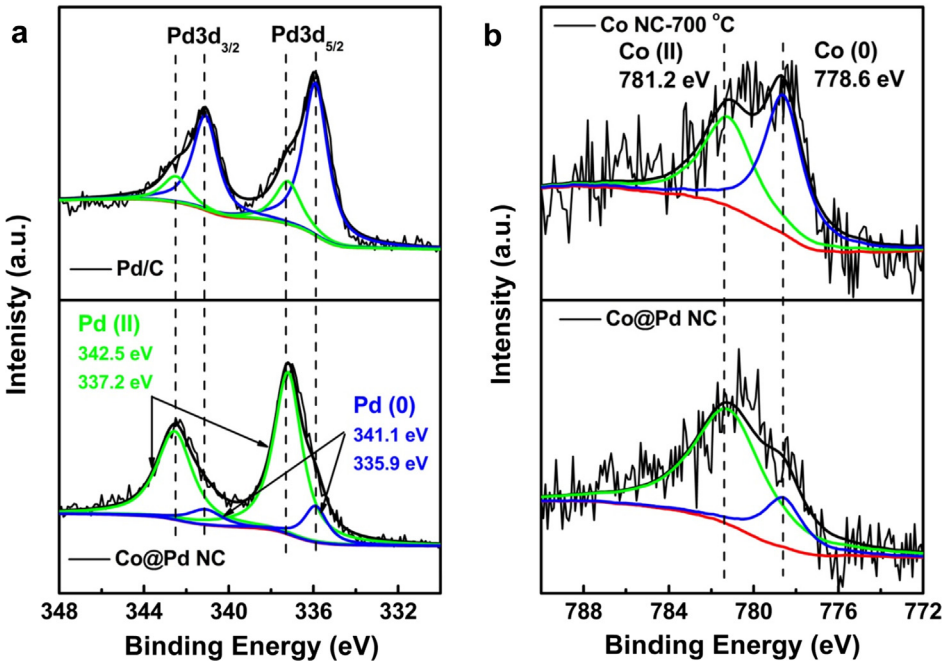

Fig. 2. (a) The XPS core-level spectra of the Pd 3d electrons in commercial Pd/C and Co@Pd NC. (b) The XPS core-level spectra of the Co $2p_{3/2}$ electrons in Co NC-700 °C and Co@Pd NC. Black curves are experimental data and colored curves are de-convoluted fittings.

Table 1
The ORR performance summary of Co NC-700 °C, Co@Pd NC and Pd/C including cathodic peak potential (E_p), onset potential (E_{onset}), diffusion-limited current density (j) at 0.5 V and Tafel slope b (mV dec^{-1}) (The tests were conducted in 0.1 M KOH). The standard deviation values were calculated based on three individual measurements.

Sample	E_p (V)	E_{onset} (V)	J (mA·cm^{-2}) at 0.5 V	Tafel slope (mV dec^{-1})
Co NC-700 °C	0.80 ± 0.01	0.95 ± 0.01	−4.66 ± 0.06	43.8 ± 0.3
Co@Pd NC	0.82 ± 0.02	0.97 ± 0.01	−6.50 ± 0.04	37.1 ± 0.5
Pd/C	0.74 ± 0.01	0.94 ± 0.02	−4.83 ± 0.08	37.3 ± 0.2

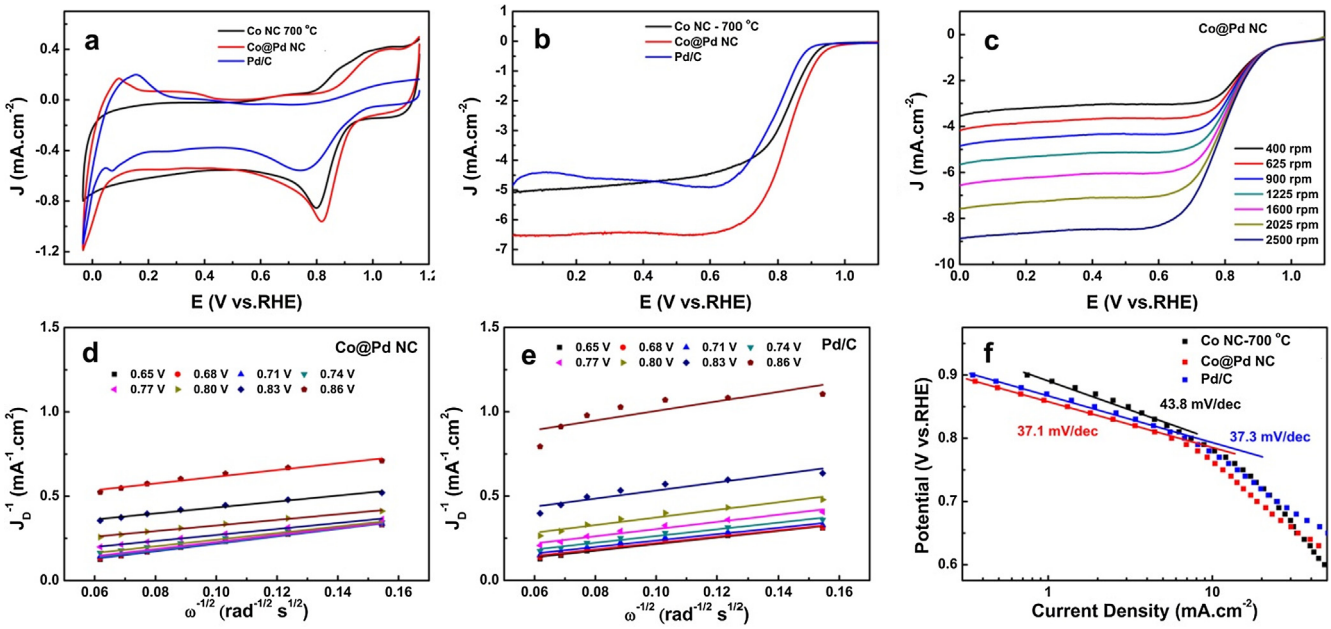

Fig. 3. (a) Cyclic and (b) RRDE voltammograms of a glassy carbon electrode modified with Co NC-700 °C, Co@Pd NC and Pd/C in O_2-saturated 0.1 M KOH solution at 1600 rpm. (c) LSV curves for Co@Pd NC samples at the rotation rates of 400–2500 rpm. The corresponding K-L plots for (d) Co@Pd NC and (e) commercial Pd/C at different electrode potentials from 0.65 V to 0.86 V. (f) The corresponding Tafel plots of Co NC-700 °C, Co@Pd NC and Commercial Pd/C catalyst. All measurements were conducted at a catalyst loading of 80.8 μg cm^{-2} in an O_2 saturated 0.1 M KOH aqueous solution at a potential scan rate of 10 mV s^{-1}.

shifted only a value of ~5 mV, much lower than the above two samples. The results imply that Co@Pd NC holds markedly superior long-term durability than Co NC-700 °C and Pd/C. In addition, the chronoamperometric measurements were conducted for the three samples to further evaluate their longevity. As presented in Fig. 4d, after continuous operation of about 8 h, the current dropped to 71.42% and 79.07% of its initial value for Co NC-700 °C and Pd/C, respectively, while under the same conditions, the current retained about 94.44% of its initial value for Co@Pd NC. The excellent performance further attests that, Co@Pd NC possessed remarkably higher long-term stability than both Co NC-700 °C and Pd/C.

3.4. The HER performance of Co@Pd NC

In addition to ORR, the electrocatalytic activity toward HER for the samples of Co NC-700 °C, Co@Pd NC and commercial Pd/C was also measured in 0.5 M H_2SO_4. The HER activity comparison is summarized in Table 2. Fig. 5 depicts the polarization curves of the three samples, and to afford a current density of 10 mA cm^{-2}, the required overpotential was −203 mV, −98 mV and −111 mV for Co NC-700 °C, Co@Pd NC and Pd/C, respectively. The overpotential value of Co@Pd NC is lower than that of Co NC-700 °C and Pd/C, suggesting that Co@Pd NC possessed higher HER activity than Co NC-700 °C and Pd/C. Tafel slope is an inherent character of an electrocatalyst, and it can be acquired by fitting the liner portion of the polarization curves with the following Tafel equation:

$$\eta = b \log j + a$$

where j is the current density and b is the Tafel slope. The Tafel plots and calculated Tafel slopes are shown in Fig. 5b. Co@Pd NC exhibited the Tafel slope of 55.7 mV dec^{-1}, much lower than that of Co NC-700 °C and Pd/C, further confirming that a much faster reaction kinetics was adopted. Subsequently, the long-term stability of Co@Pd NC for HER was tested and compared with Co NC-700 °C and Pd/C in 0.5 M H_2SO_4. Fig. 5c presents the polarization curves before and after 1000 cycles of potential scans. By employing a current density of 10 mA cm^{-2} as a metric, the required overpotential shifted about 38 eV and 39 eV for Co NC-700 °C and Pd/C, respectively, while that shift was only 10 eV for Co@Pd NC (Table 2). It suggests remarkably superior long-term durability for Co@Pd NC than Co NC-700 °C and Pd/C. Furthermore, the chronoamperometric responses toward HER in 0.5 M H_2SO_4 for all the three samples were measured. As illustrated in Fig. 5d, after continuous operation of about 10 h, the current density lost 42.0% and 64.2% of its initial value for Co NC-700 °C and Pd/C, respectively, while the current density of Co@Pd NC still remained 69.4% (30.6% loss), much higher than the above two samples (Table 2). The results further confirmed that Co@Pd NC possessed markedly superior long-term durability than Co NC-700 °C and Pd/C.

3.5. The ORR and HER performance comparison with other PdCo nanostructures

Note that, the excellent ORR and HER activities from Co@Pd NC were superior than, or at least in comparable with recently docu-

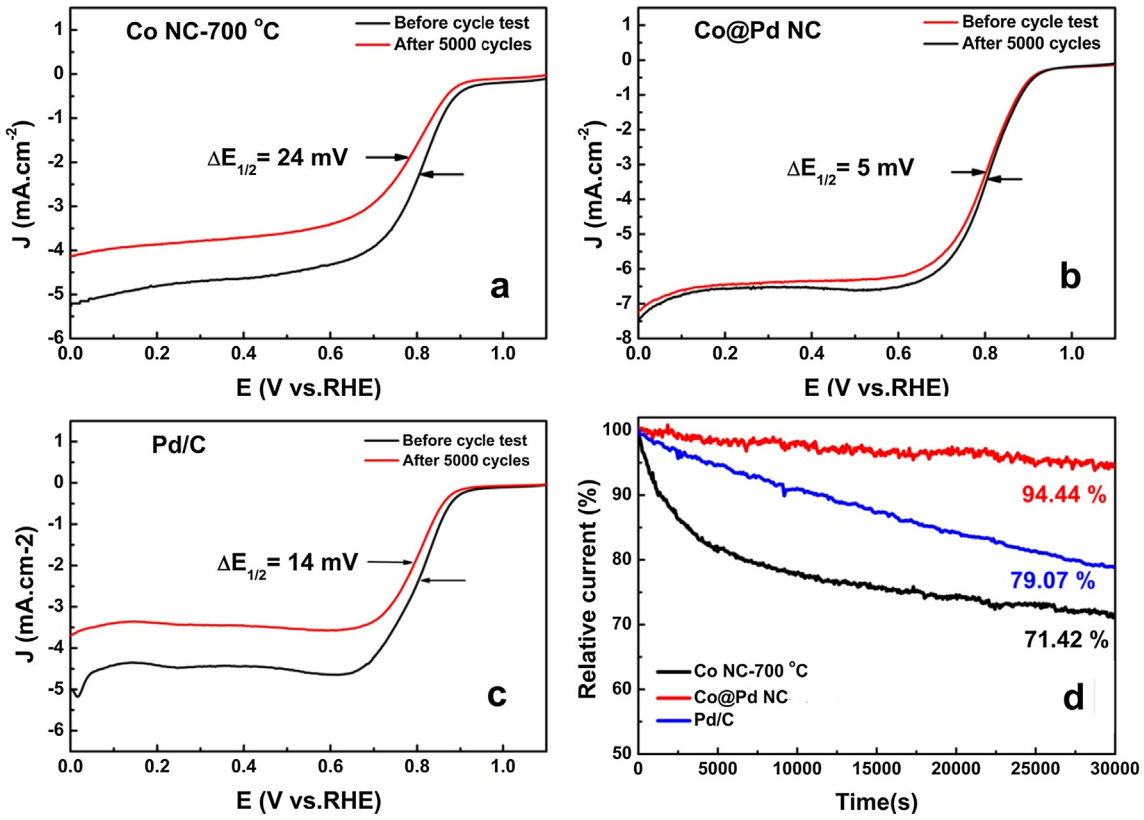

Fig. 4. The accelerated durability tests (ADT) of Co NC-700 °C (a), Co@Pd NC (b) and commercial Pd/C (c) were carried out before and after 5000 cycles between 0 and +1.1 V at a scan rate of 10 mV s^{-1} with a rotation speed of 1600 rpm in an O_2-saturated 0.1 M KOH solution. (c) Chronoamperometric responses for ORR at Co NC-700 °C, Co@Pd NC and commercial Pd/C modified electrodes in an O_2-saturated 0.1 M KOH solution at +0.5 V and 900 rpm for 30,000 s.

Table 2
The HER performance of Co NC-700 °C, Co@Pd NC and Pd/C including onset potential (E_{onset}), overpotential (E_{10}) at 10 mA·cm^{-2}, Tafel slope *b*, Overpotential negative shift ($\triangle E$) at 10 mA·cm^{-2} and the current density loss (*A%*) after chronoamperometric response for 10 h. The standard deviation values were calculated based on three individual measurements.

Sample	E_{onset} (mV)	E_{10} (mV)	*b* (mV/dec)	$\triangle E$ (mV)	*A%*
Co NC-700 °C	−40 ± 2	−203 ± 12	125.7 ± 4.5	38	42.0
Co@Pd NC	−3 ± 1	−98 ± 7	55.7 ± 2.3	10	30.6
Pd/C	−10 ± 3	−111 ± 15	96.8 ± 7.7	39	64.2

mented PdCo nanostructured catalysts under the same or similar conditions. For instance, Sridhar group employed carbon supported PdCo nanoparticles for ORR, and the best acquired potential was 0.95 V from the PdCo (3:1) sample, slightly lower than that of Co@Pd NC (0.96 V) [54]. Mech et al. prepared PdCo alloys through electrodeposition for hydrogen evolution, and the highest activity was achieved with a sample of 31.2 *at %* Pd contained [55]. Recently, Huang et al. developed a facile paragenesis strategy and successfully fabricated Pd-Co nanoparticles in nitrogen-rich carbon nanotubes to catalyze both ORR and HER. The as-synthesized Pd_{16}-CoCNTs (carbon nanotubes) showed an onset potential of 0.92 V for ORR in 0.1 M KOH, and a driven overpotential of −175 mV at the current density of 10 mA cm^{-2} for HER in 0.5 M H_2SO_4, and both values are inferior than the sample of Co@Pd NC (0.96 V & −98 mV) [56]. Note that, such impressive electrocatalytic performance was achieved with ultralow loading of Pd in Co@Pd NC, featuring the great advantages of core-shell structure with Pd as the shell.

Such impressive electrocatalytic performance can be ascribed to several factors. First of all, the Pd layer at the shell can provide abundant electrocatalytically active sites [36]; secondly, the strong synergistic effects between the Co core and Pd shell can facilitate the electron transfer kinetics during the catalytic process, as manifested by the binding energy shift observed in XPS measurements [57]; During the electrocatalytic process, the electron transfer from the Co core to the Pd shell can endow the Pd shell with stronger adsorption with the intermediates and amplify the electrocatalytic efficiency, which led to enhanced activity eventually [58,59]. Finally, rather than serving as a support, the nitrogen-doped porous carbon plays an important role in metal-nitrogen-carbon interaction. Previous investigations have demonstrated that, such metal-nitrogen-carbon interaction can lower the oxygen dissociation energy to some extent, which are favorable for accelerating ORR reaction eventually [60–62].

4. Conclusion

In summary, Co@Pd core-shell nanoparticles embedded in nitrogen-doped porous carbon have been fabricated as dual functional catalysts for both ORR and HER. Co@Pd NC exhibited much higher ORR and HER activities than commercial Pd/C catalyst. It also demonstrated remarkably higher long-term stability than Pd/C in both ORR and HER tests. The well-defined core-shell structure not only endows Co@Pd NC with excellent electrocatalytic

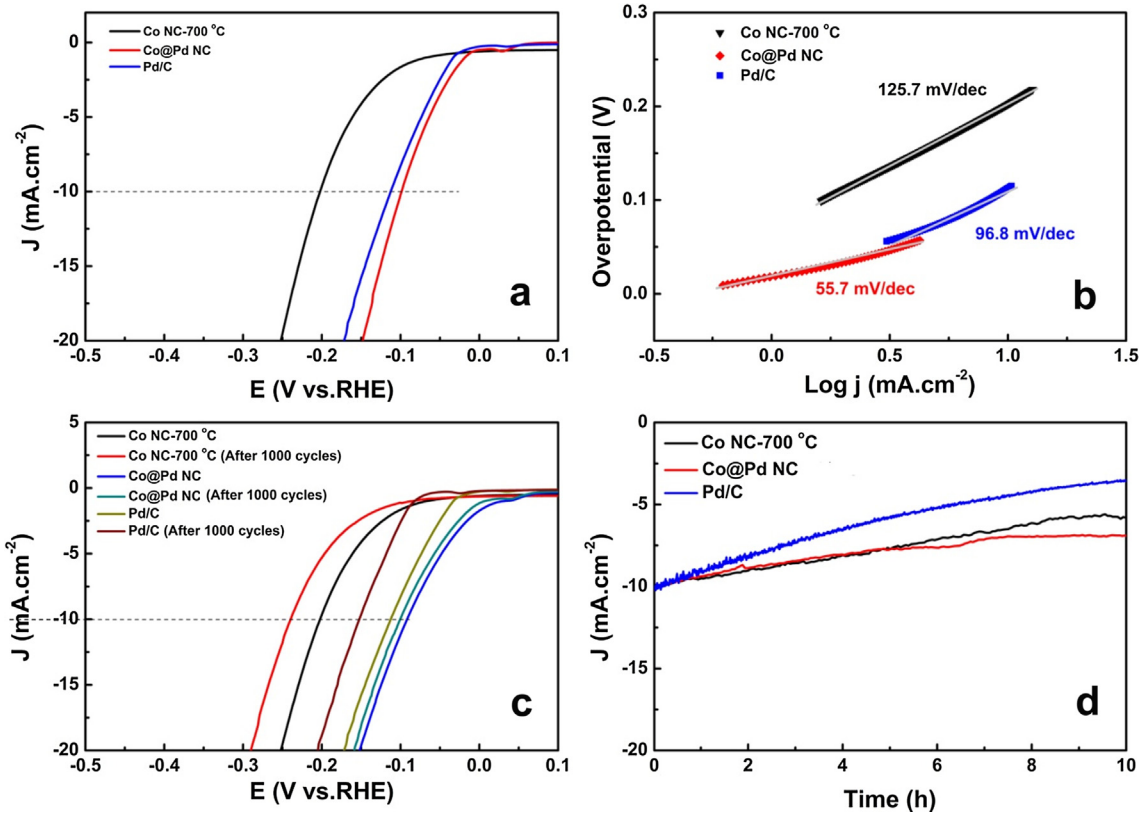

Fig. 5. (a) HER polarization curves of Co NC-700 °C, Co@Pd NC and Pd/C samples with the same mass loading. (b) The Tafel plots from Co NC-700 °C, Co@Pd NC and Pd/C samples modified electrodes. (c) The polarization curves of Co NC-700 °C, Co@Pd NC and commercial Pd/C before and after 1, 000 cycles of potential scans. (d) Chronoamperometric responses for Co NC-700 °C, Co@Pd NC and commercial Pd/C for 10 h.

performance, but also substantially enhances the atomic economy of Pd element. The combined EDX, XPS and ICP-MS results confirm that Pd content was in an ultralow atomic percentage (~1.2%), which is much lower than the previously reported Pd-based electrocatalysts [8,51,53,63–65]. The findings here provide a generic strategy for fabrication of dual functional electrocatalysts with high efficiency, low cost, and robust durability, and most importantly, ultralow noble metal loading. Further investigations on engineering the catalyst toward practical fuel cell and metal-air battery applications are underway in our lab.

Acknowledgements

This work was supported by the National Natural Science Foundation of China (No. 21501059). Z. H. T also acknowledges financial support from Science and Technology Program of Guangdong Province (No. 2017A050506014), Project of Public Interest Research and Capacity Building of Guangdong Province (No. 2015A010105009), Guangdong Innovative and Entrepreneurial Research Team Program (No. 2014ZT05N200), and Guangdong Natural Science Funds for Distinguished Young Scholars (No. 2015A030306006).

Appendix A. Supplementary material

Supplementary data associated with this article can be found, in the online version, at https://doi.org/10.1016/j.jcis.2018.05.063.

References

[1] X.-W. Liu, W.-W. Li, H.-Q. Yu, Cathodic catalysts in bioelectrochemical systems for energy recovery from wastewater, Chem. Soc. Rev. 43 (2014) 7718–7745.
[2] Y. Xu, M. Kraft, R. Xu, Metal-free carbonaceous electrocatalysts and photocatalysts for water splitting, Chem. Soc. Rev. 45 (2016) 3039–3052.
[3] Y. Li, M. Gong, Y. Liang, J. Feng, J.-E. Kim, H. Wang, G. Hong, B. Zhang, H. Dai, Advanced zinc-air batteries based on high-performance hybrid electrocatalysts, Nat. Commun. 4 (2013) 1805.
[4] M. Liu, R. Zhang, W. Chen, Graphene-supported nanoelectrocatalysts for fuel cells: synthesis, properties, and applications, Chem. Rev. 114 (2014) 5117–5160.
[5] M. Shao, Q. Chang, J.-P. Dodelet, R. Chenitz, Recent advances in electrocatalysts for oxygen reduction reaction, Chem. Rev. 116 (2016) 3594–3657.
[6] Yiliguma, Y. Tang, G. Zheng, Colloidal nanocrystals for electrochemical reduction reactions, J. Colloid Interface Sci. 485 (2017) 308–327.
[7] D. Strmcnik, P.P. Lopes, B. Genorio, V.R. Stamenkovic, N.M. Markovic, Design principles for hydrogen evolution reaction catalyst materials, Nano Energy 29 (2016) 29–36.
[8] L. Zhang, Q. Chang, H. Chen, M. Shao, Recent advances in palladium-based electrocatalysts for fuel cell reactions and hydrogen evolution reaction, Nano Energy 29 (2016) 198–219.
[9] Y. Wang, L. Chen, X. Yu, Y. Wang, G. Zheng, Superb Alkaline hydrogen evolution and simultaneous electricity generation by Pt-decorated Ni_3N nanosheets, Adv. Energy Mater. 7 (2017) 1601390.
[10] M. Kuang, G. Zheng, Nanostructured bifunctional redox electrocatalysts, Small 12 (2016) 5656–5675.
[11] L. Bu, N. Zhang, S. Guo, X. Zhang, J. Li, J. Yao, T. Wu, G. Lu, J.-Y. Ma, D. Su, X. Huang, Biaxially strained PtPb/Pt core/shell nanoplate boosts oxygen reduction catalysis, Science 354 (2016) 1410–1414.
[12] J. Wu, H. Yang, Platinum-based oxygen reduction electrocatalysts, Acc. Chem. Res. 46 (2013) 1848–1857.
[13] J. Wang, F. Xu, H. Jin, Y. Chen, Y. Wang, Non-noble metal-based carbon composites in hydrogen evolution reaction: fundamentals to applications, Adv. Mater. 29 (2017) 1605838.
[14] P.-Q. Liao, N.-Y. Huang, W.-X. Zhang, J.-P. Zhang, X.-M. Chen, Controlling guest conformation for efficient purification of butadiene, Science 356 (2017) 1193–1196.
[15] Y.-P. Chen, Y. Liu, D. Liu, M. Bosch, H.-C. Zhou, direct measurement of adsorbed gas redistribution in metal-organic frameworks, J. Am. Chem. Soc. 137 (2015) 2919–2930.
[16] R.W. Flaig, T.M. Osborn Popp, A.M. Fracaroli, E.A. Kapustin, M.J. Kalmutzki, R.M. Altamimi, F. Fathieh, J.A. Reimer, O.M. Yaghi, The chemistry of CO_2 capture in an amine-functionalized metal-organic framework under dry and humid conditions, J. Am. Chem. Soc. 139 (2017) 12125–12128.
[17] L. Zhu, X.-Q. Liu, H.-L. Jiang, L.-B. Sun, Metal-organic frameworks for heterogeneous basic catalysis, Chem. Rev. 117 (2017) 8129–8176.

[18] M. Zhao, K. Yuan, Y. Wang, G. Li, J. Guo, L. Gu, W. Hu, H. Zhao, Z. Tang, Metal–organic frameworks as selectivity regulators for hydrogenation reactions, Nature 539 (2016) 76–80.
[19] R.V. Jagadeesh, K. Murugesan, A.S. Alshammari, H. Neumann, M.-M. Pohl, J. Radnik, M. Beller, MOF-derived cobalt nanoparticles catalyze a general synthesis of amines, Science 358 (2017) 326–332.
[20] H. Zheng, Y. Zhang, L. Liu, W. Wan, P. Guo, A.M. Nyström, X. Zou, One-pot synthesis of metal-organic frameworks with encapsulated target molecules and their applications for controlled drug delivery, J. Am. Chem. Soc. 138 (2016) 962–968.
[21] L. Chen, R. Luque, Y. Li, Controllable design of tunable nanostructures inside metal-organic frameworks, Chem. Soc. Rev. 46 (2017) 4614–4630.
[22] S.-L. Li, Q. Xu, Metal-organic frameworks as platforms for clean energy, Energy. Environ. Sci. 6 (2013) 1656–1683.
[23] W. Xia, A. Mahmood, R. Zou, Q. Xu, Metal-organic frameworks and their derived nanostructures for electrochemical energy storage and conversion, Energy. Environ. Sci. 8 (2015) 1837–1866.
[24] W. Liu, X.-B. Yin, Metal–organic frameworks for electrochemical applications, Trend Anal. Chem. 75 (2016) 86–96.
[25] Z. Liang, C. Qu, W. Guo, R. Zou, Q. Xu, Pristine metal-organic frameworks and their composites for energy storage and conversion, Adv. Mater. 1702891 (2017).
[26] Q.-L. Zhu, W. Xia, T. Akita, R. Zou, Q. Xu, Metal-organic framework-derived honeycomb-like open porous nanostructures as precious-metal-free catalysts for highly efficient oxygen electroreduction, Adv. Mater. 28 (2016) 6391–6398.
[27] H. Tabassum, W. Guo, W. Meng, A. Mahmood, R. Zhao, Q. Wang, R. Zou, Metal-organic frameworks derived cobalt phosphide architecture encapsulated into B/N Co-doped graphene nanotubes for all pH value electrochemical hydrogen evolution, Adv. Energy Mater. 7 (2017) 1601671.
[28] A. Mahmood, W. Guo, H. Tabassum, R. Zou, Metal-organic framework-based nanomaterials for electrocatalysis, Adv. Energy Mater. 6 (2016) 1600423.
[29] B.Y. Xia, Y. Yan, N. Li, H.B. Wu, X.W. Lou, X. Wang, A metal–organic framework-derived bifunctional oxygen electrocatalyst, Nat. Energy 1 (2016) 15006.
[30] L. Zhang, X. Wang, R. Wang, M. Hong, Structural evolution from metal-organic framework to hybrids of nitrogen-doped porous carbon and carbon nanotubes for enhanced oxygen reduction activity, Chem. Mater. 27 (2015) 7610–7618.
[31] Q. Li, H. Pan, D. Higgins, R. Cao, G. Zhang, H. Lv, K. Wu, J. Cho, G. Wu, Metal-organic framework-derived bamboo-like nitrogen-doped graphene tubes as an active matrix for hybrid oxygen-reduction electrocatalysts, Small 11 (2015) 1443–1452.
[32] Q. Lai, Y. Zhao, Y. Liang, J. He, J. Chen, In Situ confinement pyrolysis transformation of ZIF-8 to nitrogen-enriched meso-microporous carbon frameworks for oxygen reduction, Adv. Funct. Mater. 26 (2016) 8334–8344.
[33] H.B. Wu, B.Y. Xia, L. Yu, X.-Y. Yu, X.W. Lou, Porous molybdenum carbide nano-octahedrons synthesized via confined carburization in metal-organic frameworks for efficient hydrogen production, Nat. Commun. 6 (2015) 6512.
[34] M. Kuang, Q. Wang, P. Han, G. Zheng, Cu, Co-embedded N-enriched mesoporous carbon for efficient oxygen reduction and hydrogen evolution reactions, Adv. Energy Mater. 7 (2017) 1700193.
[35] L. Wang, Z. Tang, W. Yan, Q. Wang, H. Yang, S. Chen, Co@Pt Core@Shell nanoparticles encapsulated in porous carbon derived from zeolitic imidazolate framework 67 for oxygen electroreduction in alkaline media, J. Power Sources 343 (2017) 458–466.
[36] K. Shen, L. Chen, J. Long, W. Zhong, Y. Li, MOFs-templated Co@Pd Core-Shell NPs embedded in N-doped carbon matrix with superior hydrogenation activities, ACS Catal. 5 (2015) 5264–5271.
[37] R. Banerjee, A. Phan, B. Wang, C. Knobler, H. Furukawa, M. O'Keeffe, O.M. Yaghi, High-throughput synthesis of zeolitic imidazolate frameworks and application to CO_2 capture, Science 319 (2008) 939–943.
[38] J. Qian, F. Sun, L. Qin, Hydrothermal synthesis of zeolitic imidazolate framework-67 (ZIF-67) nanocrystals, Mater. Lett. 82 (2012) 220–223.
[39] D. Li, Z. Zong, Z. Tang, Z. Liu, S. Chen, Y. Tian, X. Wang, Total water splitting catalyzed by Co@Ir Core-Shell nanoparticles encapsulated in nitrogen-doped porous carbon derived from metal-organic frameworks, ACS Sustain. Chem. Eng. 6 (2018) 5105–5114.
[40] K.M. Nam, J.H. Shim, H. Ki, S.-I. Choi, G. Lee, J.K. Jang, Y. Jo, M.-H. Jung, H. Song, J.T. Park, Single-crystalline hollow face-centered-cubic cobalt nanoparticles from solid face-centered-cubic cobalt oxide nanoparticles, Angew. Chem. Int. Ed. 47 (2008) 9504–9508.
[41] J. Wu, S. Shan, V. Petkov, B. Prasai, H. Cronk, P. Joseph, J. Luo, C.-J. Zhong, Composition–structure–activity relationships for palladium-alloyed nanocatalysts in oxygen reduction reaction: an ex-situ/in-situ high energy X-ray diffraction study, ACS Catal. 5 (2015) 5317–5327.
[42] M. Shao, J. Odell, M. Humbert, T. Yu, Y. Xia, Electrocatalysis on shape-controlled palladium nanocrystals: oxygen reduction reaction and formic acid oxidation, J. Phys. Chem. C 117 (2013) 4172–4180.
[43] J. Wu, S. Shan, J. Luo, P. Joseph, V. Petkov, C.-J. Zhong, PdCu Nanoalloy electrocatalysts in oxygen reduction reaction: role of composition and phase state in catalytic synergy, ACS Appl. Mater. Interfaces 7 (2015) 25906–25913.
[44] X. Wang, J. Zhou, H. Fu, W. Li, X. Fan, G. Xin, J. Zheng, X. Li, MOF derived catalysts for electrochemical oxygen reduction, J. Mater. Chem. A 2 (2014) 14064–14070.
[45] N. Alexeyeva, A. Sarapuu, K. Tammeveski, F.J. Vidal-Iglesias, J. Solla-Gullón, J.M. Feliu, Electroreduction of oxygen on Vulcan carbon supported Pd nanoparticles and Pd–M nanoalloys in acid and alkaline solutions, Electrochim. Acta 56 (2011) 6702–6708.
[46] M. Lüsi, H. Erikson, A. Sarapuu, K. Tammeveski, J. Solla-Gullón, J.M. Feliu, Oxygen reduction reaction on carbon-supported palladium nanocubes in alkaline media, Electrochem. Commun. 64 (2016) 9–13.
[47] H. Yang, Z. Tang, W. Yan, L. Wang, Q. Wang, Y. Zhang, Z. Liu, S. Chen, Peptide capped Pd nanoparticles for oxygen electroreduction: strong surface effects, J. Alloys. Compd. 702 (2017) 146–152.
[48] S.-S. Li, J.-N. Zheng, A.-J. Wang, F.-L. Tao, J.-J. Feng, J.-R. Chen, H. Yu, Branched platinum-on-palladium bimetallic heteronanostructures supported on reduced graphene oxide for highly efficient oxygen reduction reaction, J. Power Sources 272 (2014) 1078–1085.
[49] J.-J. Lv, J.-N. Zheng, Y.-Y. Wang, A.-J. Wang, L.-L. Chen, J.-J. Feng, A simple one-pot strategy to platinum–palladium@palladium core–shell nanostructures with high electrocatalytic activity, J. Power Sources 265 (2014) 231–238.
[50] C. Song, J. Zhang, PEM fuel cell electrocatalysis and catalyst layers: fundamentals and applications, 2008th Edition, Springer, 2008 pp. 89–134.
[51] W. Yan, Z. Tang, L. Li, L. Wang, H. Yang, Q. Wang, W. Wu, S. Chen, Ultrasmall palladium nanoclusters encapsulated in porous carbon nanosheets for oxygen electroreduction in alkaline media, ChemElectroChem 4 (2017) 1349–1355.
[52] C.P. Deming, R. Mercado, V. Gadiraju, S.W. Sweeney, M. Khan, S. Chen, Graphene quantum dots-supported palladium nanoparticles for efficient electrocatalytic reduction of oxygen in alkaline media, ACS Sustain. Chem. Eng. 3 (2015) 3315–3323.
[53] C.P. Deming, R. Mercado, J.E. Lu, V. Gadiraju, M. Khan, S. Chen, Oxygen electroreduction catalyzed by palladium nanoparticles supported on nitrogen-doped graphene quantum dots: impacts of nitrogen dopants, ACS Sustain. Chem. Eng. 4 (2016) 6580–6589.
[54] S. Maheswari, S. Karthikeyan, P. Murugan, P. Sridhar, S. Pitchumani, Carbon-supported Pd-Co as cathode catalyst for APEMFCs and validation by DFT, Phys. Chem. Chem. Phys. 14 (2012) 9683–9695.
[55] K. Mech, P. Żabiński, R. Kowalik, T. Tokarski, K. Fitzner, Electrodeposition of Co–Pd alloys from ammonia solutions and their catalytic activity for hydrogen evolution reaction, J. Appl. Electrochem. 44 (2014) 97–103.
[56] B. Huang, L. Chen, Y. Wang, L. Ouyang, J. Ye, Paragenesis of palladium-cobalt nanoparticle in nitrogen-rich carbon nanotubes as a bifunctional electrocatalyst for hydrogen-evolution reaction and oxygen-reduction reaction, Chem. Eur. J. 23 (2017) 7710–7718.
[57] W. Tang, G. Henkelman, Charge redistribution in core-shell nanoparticles to promote oxygen reduction, J. Chem. Phys. 130 (2009) 194504.
[58] X.-X. Lin, A.-J. Wang, K.-M. Fang, J. Yuan, J.-J. Feng, One-Pot seedless aqueous synthesis of reduced graphene oxide (rGO)-supported core-shell Pt@Pd nanoflowers as advanced catalysts for oxygen reduction and hydrogen evolution, ACS Sustain. Chem. Eng. 5 (2017) 8675–8683.
[59] T.D. Thanh, N.D. Chuong, H.V. Hien, N.H. Kim, J.H. Lee, CuAg@Ag core-shell nanostructure encapsulated by N-doped graphene as a high-performance catalyst for oxygen reduction reaction, ACS Appl. Mater. Interfaces 10 (2018) 4672–4681.
[60] W. Niu, L. Li, X. Liu, N. Wang, J. Liu, W. Zhou, Z. Tang, S. Chen, Mesoporous N-doped carbons prepared with thermally removable nanoparticle templates: an efficient electrocatalyst for oxygen reduction reaction, J. Am. Chem. Soc. 137 (2015) 5555–5562.
[61] W.-J. Jiang, L. Gu, L. Li, Y. Zhang, X. Zhang, L.-J. Zhang, J.-Q. Wang, J.-S. Hu, Z. Wei, L.-J. Wan, Understanding the high activity of Fe–N–C electrocatalysts in oxygen reduction: Fe/Fe_3C nanoparticles boost the activity of Fe–N_x, J. Am. Chem. Soc. 138 (2016) 3570–3578.
[62] S. Gupta, S. Zhao, O. Ogoke, Y. Lin, H. Xu, G. Wu, Engineering favorable morphology and structure of Fe-N-C oxygen-reduction catalysts through tuning of nitrogen/carbon precursors, ChemSusChem 10 (2017) 774–785.
[63] H. Begum, M.S. Ahmed, S. Cho, S. Jeon, Freestanding palladium nanonetworks electrocatalyst for oxygen reduction reaction in fuel cells, Int. J. Hydrogen Energy 43 (2018) 229–238.
[64] Y. Zuo, D. Rao, S. Li, T. Li, G. Zhu, S. Chen, L. Song, Y. Chai, H. Han, Atomic vacancies control of Pd-based catalysts for enhanced electrochemical performance, Adv. Mater. 30 (2018).
[65] T. Li, Z. Tang, K. Wang, W. Wu, S. Chen, C. Wang, Palladium nanoparticles grown on β-Mo2C nanotubes as dual functional electrocatalysts for both oxygen reduction reaction and hydrogen evolution reaction, Int. J. Hydrogen Energy 43 (2018) 4932–4941.